


Cite this: *RSC Adv.*, 2025, 15, 17089

# Facile preparation of a 3D rGO/g-C<sub>3</sub>N<sub>4</sub> nanocomposite loaded with Ag NPs for photocatalytic degradation

Kesheng Cao,<sup>a</sup> Xueyu Ge,<sup>a</sup> Shuang Li,<sup>a</sup> Zhengshan Tian,<sup>\*a</sup> Suyu Cui,<sup>a</sup> Guijin Guo,<sup>a</sup> Liuqing Yang,<sup>a</sup> Xingwu Li,<sup>a</sup> Yabo Wang,<sup>a</sup> Suzhen Bai,<sup>a</sup> Qian Wei<sup>\*b</sup> and Wei Li<sup>id</sup><sup>\*b</sup>

Graphene-based and g-C<sub>3</sub>N<sub>4</sub>-based nanocomposites can effectively remove organic pollutants from water. However, the reasonable design and scale preparation of hybrid nanomaterials of reduced graphene oxide (rGO), g-C<sub>3</sub>N<sub>4</sub> and silver nanoparticles (Ag NPs) with improved performance for practical application need to be further explored. Herein, a 3D rGO/g-C<sub>3</sub>N<sub>4</sub> nanocomposite loaded with Ag NPs was successfully fabricated through a facile three-step synthetic route. The microstructure and morphology of GO, g-C<sub>3</sub>N<sub>4</sub>, rGO/g-C<sub>3</sub>N<sub>4</sub> and rGO/g-C<sub>3</sub>N<sub>4</sub> nanocomposite loaded with Ag NPs were characterized and analyzed. The experimental results show that the as-prepared nanocomposite loaded with Ag NPs has excellent activity to remove methylene blue (MB) from water under visible light irradiation, and its maximum removal capacity is high as 49.60 mg g<sup>-1</sup> within 60 min. Based on its possible catalytic process and kinetic analysis, the adsorption and catalytic performance of this nanocomposite may be attributed to a synergistic effect of rGO, g-C<sub>3</sub>N<sub>4</sub> and Ag NPs. In addition, it can provide a useful reference for the rational design and scale preparation of rGO/g-C<sub>3</sub>N<sub>4</sub> nanocomposite for practical applications.

Received 7th April 2025

Accepted 14th May 2025

DOI: 10.1039/d5ra02399h

rsc.li/rsc-advances

## 1. Introduction

At present, organic pollutants in water can cause a serious threat to human health and the safety of the ecological environment.<sup>1,2</sup> Moreover, organic dyes and aromatic compounds are generally recognized as the main organic pollutants in water.<sup>3,4</sup> To solve this problem, numerous approaches have been employed to remove organic pollutants from water.<sup>1–5</sup> Among them, adsorption and photocatalytic degradation are generally considered as efficient methods, especially graphene-based and g-C<sub>3</sub>N<sub>4</sub>-based nanocomposites have attracted extensive research attention.<sup>3–7</sup>

On the one hand, graphene as a 2D nanocarbon material, has lots of novel functional applications due to its high strength, high conductivity and large specific surface area and so on.<sup>8–10</sup> Graphene-based nanomaterials are generally used as excellent adsorbents and catalysts owing to their excellent physical and chemical properties.<sup>11–14</sup> However, graphene has no functional groups (such as carboxyl group, hydroxyl group and epoxy group) on its surface, and van der Waals forces lead

to easy agglomerate between different layers,<sup>15,16</sup> thus it is very difficult to interact with other molecules or ions, which hinders its practical functional application.

On the other hand, graphene oxide (GO), as a derivative of graphene, has some advantages such as rich pore structure and some oxygen-containing groups on its surface.<sup>17–19</sup> Importantly, these oxygen-containing groups can provide numerous reactive sites to enhance interactions with other molecules or ions.<sup>20–22</sup> Moreover, the negatively charged GO with excellent hydrophilicity can strongly adsorb heavy metal cations and cationic dyes in wastewater through electrostatic actions and  $\pi$ - $\pi$  interactions.<sup>23–25</sup>

At the same time, to improve the adsorption and catalytic performance of GO, it is usually hybridized to prepare GO-based nanocomposites, especially nanomaterials hybridized with Ag NPs have attracted intense attention because of their excellent performance.<sup>26–28</sup> For example, Rath and co-workers<sup>28</sup> designed GO/Ag nanocomposite to adsorb crystal violet dye at pH of 8, and the maximum adsorption capacity of crystal violet was as high as 48.78 mg g<sup>-1</sup>. Moreover, after many adsorption and desorption cycles, its recyclability and stability were also satisfactory. Naeem and co-workers<sup>4</sup> prepared GO/Ag nanocomposite not only as adsorbent to adsorb multiple pollutants, but also as catalyst to catalyze the degradation of dyes. Mohamed and co-workers<sup>29</sup> designed rGO impregnated with Ag NPs to catalyze the degradation of MB, and this nanocomposite of rGO with Ag NPs was efficiently used as adsorbent and

<sup>a</sup>School of Chemistry and Environmental Engineering, Henan Province Engineering Technology Research Center of Green Hydrogen & Electrochemical Energy Storage, Pingdingshan University, Pingdingshan, 467000, China. E-mail: tianzhengshan@163.com

<sup>b</sup>College of Optical, Mechanical and Electrical Engineering, Zhejiang A&F University, Hangzhou, 311300, China. E-mail: qweiyk@126.com; liuwei@zafu.edu.cn



catalyst to remove organic dyes because of its excellent electrical conductivity and highly catalytic active feature of Ag NPs.

Recently, graphitic carbon nitride ( $g\text{-C}_3\text{N}_4$ ), as a novel 2D graphene analogue, has emerged as a promising photocatalyst since 2009 (ref. 30) due to its excellent physical and chemical properties such as tunable band structure, non-toxicity, facile synthesis and chemical stability.<sup>31–33</sup> However, the pristine  $g\text{-C}_3\text{N}_4$  catalyst still has some inherent disadvantages such as its poor charge separation, limited light absorption and low surface area, thus leading to its moderate photocatalytic activity.<sup>34–36</sup>

To improve the photocatalytic performance of  $g\text{-C}_3\text{N}_4$ -based photocatalysts, some further modification strategies (such as vacancy engineering, nanostructure design, heteroatom doping and forming heterostructure) have been attempted.<sup>37</sup> Particularly,  $g\text{-C}_3\text{N}_4$  with 3D nanostructure can increase the specific surface area and improve the anchoring stability of cocatalysts. Moreover, graphene with 3D nanostructure can promote light absorption and enhance charge migration.<sup>38</sup> because graphene acts as a light-transmitting material and a conductor.<sup>39</sup> At the same time, the loaded cocatalysts can be used as the electron acceptors to remarkably promote the electron-hole separation.<sup>37</sup>

More recently, many efforts have been focused on the internal electrons of  $g\text{-C}_3\text{N}_4$  at the atomic scale through monatomic engineering.<sup>40–43</sup> The metal atoms can be uniformly anchored on the network by forming coordination bonds with lone pair electrons of the nitrogen contained in  $g\text{-C}_3\text{N}_4$ . Specifically, Ag NPs dispersed in the  $g\text{-C}_3\text{N}_4$  nanosheets can significantly accelerate the charge separation to improve the photocatalytic activity.<sup>44,45</sup> For example, Jiang and co-workers<sup>40</sup> designed the  $g\text{-C}_3\text{N}_4$  catalyst anchored with Ag NPs, which exhibited excellent catalytic activity and durability for efficient photocatalytic hydrogen evolution, because the Ag NPs not only extend the visible light absorption region but also facilitate electron transfer.<sup>41–43</sup>

Although numerous results of  $g\text{-C}_3\text{N}_4$ -based photocatalysts have been achieved, however, to overcome their serious drawbacks such as small specific surface area, fast charge recombination and limited visible-light absorption,<sup>46,47</sup> the reasonable design of  $g\text{-C}_3\text{N}_4$ -based photocatalysts with rGO and Ag NPs is still a research hotspot. In particular, Ag doping can not only enhance the light absorption but also accelerate the photo-generated carrier transfer process, and its related mechanism needs to be given intensified attention. Therefore, the reasonable design and scale preparation of hybrid nanomaterials of rGO,  $g\text{-C}_3\text{N}_4$  and Ag NPs with improved performance for practical applications need to be further explored.

In this paper, we successfully fabricated a 3D rGO/ $g\text{-C}_3\text{N}_4$  nanocomposite loaded with Ag NPs (rGO/ $g\text{-C}_3\text{N}_4$ /Ag NPs) through a facile three-step synthetic route. At the same time, the adsorption and catalytic properties of this nanocomposite were analyzed. Moreover, its possible catalytic process and kinetic analysis were discussed.

## 2. Experimental section

### 2.1 Materials and reagents

All the chemicals were of analytical grade and purchased from National Pharmaceutical Reagent Company, including graphite powders (99.5 wt% purity, 200 mesh), concentrated sulfuric acid ( $\text{H}_2\text{SO}_4$ , 98 wt%), sodium nitrate ( $\text{NaNO}_3$ ), potassium permanganate ( $\text{KMnO}_4$ ), hydrogen peroxide ( $\text{H}_2\text{O}_2$ , 30 wt%), sodium chloride ( $\text{NaCl}$ ), silver nitrate ( $\text{AgNO}_3$ ), ammonia ( $\text{NH}_3 \cdot \text{H}_2\text{O}$ ), methylene blue (MB), melamine and glucose. All the chemicals were used without further purification. Deionized water (a resistance of 18 M $\Omega$ ) made from a Milli-Q solvent system in our own lab was used through all the experiments.

### 2.2 Methods

**2.2.1 Synthesis of GO sheets.** GO was prepared from natural graphite powders based on the oxidation intercalation of the improved Hummers' method<sup>18,19,48</sup> and subsequent exfoliation under ultrasound.<sup>49–51</sup> As a typical process, firstly, 10.0 g of graphite powders, 5.0 g of  $\text{NaNO}_3$  and 240 mL of  $\text{H}_2\text{SO}_4$  (98 wt%) were mixed in a beaker under an ice-water bath with electromagnetic stirring for 30 min. Secondly, 30.0 g of  $\text{KMnO}_4$  was slowly added to the mixture under an ice-water bath, and this addition was completed within 30 min under electromagnetic stirring. Thirdly, the obtained mixture was stirred for 3 h at room temperature, and 300 mL of deionized water was slowly added into the above mixture, keeping stirring for 1 h. Fourthly, 35 mL of  $\text{H}_2\text{O}_2$  (30 wt%) was dropped into the above mixture to eliminate unreacted  $\text{KMnO}_4$  under stirring, and then graphite oxide was obtained after the precipitate was washed with deionized water several times. Fifthly, an aqueous suspension of GO sheets was prepared by ultrasonic stripping of graphite oxide in deionized water for 2 h. Finally, a sample of GO powders was obtained after GO suspension was dried in a vacuum drying oven at 60 °C for 24 h.

**2.2.2 Preparation of  $g\text{-C}_3\text{N}_4$  sheets.** The bulk  $g\text{-C}_3\text{N}_4$  powders were synthesized by calcinating a mixture of melamine and NaCl based on a thermal polymerization reaction.<sup>52</sup> Typically, firstly, 10.0 g of melamine and 8.0 g of NaCl were mixed and evenly ground, and then placed in a porcelain crucible with a cover. Subsequently, the mixture in the crucible was placed in the muffle furnace and heated to 550 °C with a heating rate of 5 °C min<sup>−1</sup>, keeping at this temperature for 5 h. Thirdly, the sample in the crucible was naturally cooled to room temperature, after several washing with deionized water to remove NaCl, the product of bulk  $g\text{-C}_3\text{N}_4$  powders was dried and ground into fine powders for characterization and use. Finally, the  $g\text{-C}_3\text{N}_4$  sheets were prepared by sonicating fine  $g\text{-C}_3\text{N}_4$  powders in deionized water for 2 h. As control experiments, the samples of 500 °C and 600 °C were prepared by only changing the thermal polymerization reaction temperature. These preparation processes were easily operated under ambient conditions, and no inert gas protection was required.

**2.2.3 Preparation of rGO/ $g\text{-C}_3\text{N}_4$  nanocomposite.** The GO/ $g\text{-C}_3\text{N}_4$  nanocomposite was fabricated *via* a simple ultrasound-assisted method. Typically, 0.1 g of GO powders was dispersed



in 100 mL of deionized water and sonicated for 2 h to produce a GO suspension ( $1 \text{ mg mL}^{-1}$ ). Similarly, 0.1 g of fine  $\text{g-C}_3\text{N}_4$  powders was dispersed in 100 mL of deionized water to obtain  $\text{g-C}_3\text{N}_4$  suspension ( $1 \text{ mg mL}^{-1}$ ) through an ultrasonic process. Subsequently, the obtained  $\text{g-C}_3\text{N}_4$  suspension was slowly added into the above GO suspension under ultrasound for 30 min to fabricate  $\text{GO/g-C}_3\text{N}_4$  nanocomposite. Thirdly, the obtained  $\text{GO/g-C}_3\text{N}_4$  nanocomposite was placed in a high-pressure reactor and heated to  $200^\circ\text{C}$ , keeping for 5 h. After cooling to room temperature, the sample was taken out from the high-pressure reactor. Finally, a sample of  $\text{rGO/g-C}_3\text{N}_4$  nanocomposite was obtained after being filtered and dried, which can be used for subsequent use.

On the basis of the as-prepared GO and  $\text{g-C}_3\text{N}_4$  suspension, GO nanosheets with excellent hydrophilicity can be evenly dispersed in an aqueous solution, and they are beneficial to interact with  $\text{g-C}_3\text{N}_4$  nanosheets to form  $\text{GO/g-C}_3\text{N}_4$  nanocomposite.<sup>53,54</sup> Moreover, during the hydrothermal reaction, GO and  $\text{g-C}_3\text{N}_4$  nanosheets can be self-assembled to  $\text{rGO/g-C}_3\text{N}_4$  nanocomposite with 3D network structure, similar to the self-assembly of GO nanosheets.<sup>55</sup>

**2.2.4 Preparation of  $\text{rGO/g-C}_3\text{N}_4/\text{Ag}$  NPs.** An appropriate amount of  $\text{rGO/g-C}_3\text{N}_4$  nanocomposite was dispersed in deionized water under ultrasound, and a solution of silver ammonium complex ion was slowly added to the dispersion of  $\text{rGO/g-C}_3\text{N}_4$  nanocomposite under stirring. Subsequently, an aqueous solution of glucose (5 wt%) was added to the above mixture under  $70^\circ\text{C}$  water bath with ultrasound. After 30 min, the  $\text{rGO/g-C}_3\text{N}_4$  nanocomposite was *in situ* loaded with Ag NPs. After several washing with deionized water, the sample was filtered and dried in a vacuum drying oven at  $60^\circ\text{C}$  for 24 h for characterization and use.

## 2.3 Characterizations

Their microstructure and morphology of GO,  $\text{g-C}_3\text{N}_4$ ,  $\text{rGO/g-C}_3\text{N}_4$  and  $\text{rGO/g-C}_3\text{N}_4/\text{Ag}$  NPs were detected by the scanning electron microscopy (SEM, Hitachi S-4800) and transmission electron microscopy (TEM, JEM-2100). Fourier transform infrared spectroscopy (FTIR, Nicolet5700), Raman spectroscopy (M00-141) and X-ray diffractometer (XRD, Bruker D8 diffractometer) were used to analyze structural compositions of the relevant samples.

# 3. Results and discussion

## 3.1 Structure analysis

Three steps were rationally designed to fabricate  $\text{rGO/g-C}_3\text{N}_4/\text{Ag}$  NPs, and a schematic procedure was shown in Fig. 1. After the ultrasonic stripping of  $\text{g-C}_3\text{N}_4$  powders in deionized water, an aqueous suspension of  $\text{g-C}_3\text{N}_4$  nanosheets can be prepared, and its color is milky yellow (Fig. 1a). Subsequently, an aqueous suspension of  $\text{g-C}_3\text{N}_4$  nanosheets was gradually added to an aqueous suspension of GO (Fig. 1b) under ultrasonic treatment. Then, a nanocomposite of  $\text{GO/g-C}_3\text{N}_4$  was easily obtained, which has a milky grey colour, as shown in Fig. 1. After a hydrothermal reaction in a high pressure reactor at  $200^\circ\text{C}$  for

5 h, the above  $\text{GO/g-C}_3\text{N}_4$  nanocomposite was transformed into  $\text{rGO/g-C}_3\text{N}_4$  nanocomposite, as shown in Fig. 1d. Finally, the  $\text{rGO/g-C}_3\text{N}_4$  nanocomposite was *in situ* loaded Ag NPs to fabricate 3D nanocomposite hybridized with Ag NPs, as shown in Fig. 1e and f.

The  $\text{rGO/g-C}_3\text{N}_4/\text{Ag}$  NPs mainly consists of three active ingredients ( $\text{rGO}$ ,  $\text{g-C}_3\text{N}_4$  and Ag NPs), which are effectively combined together. Each of them has a very important role in the nanocomposite for functional applications, and thus each ingredient needs to be considered in the preparation process in detail.

Based on the improved Hummers' method<sup>18,19,48</sup> and subsequent ultrasonic stripping,<sup>49–51</sup> the graphite powders were converted into GO sheets, accompanied with a slight color changing from dark black to grey black, as shown in Fig. 2a and b. The obtained GO sheets are single layer or several layers with loose, stacked and cross-linked structure, as displayed in Fig. 2c and d.

The microstructure of  $\text{g-C}_3\text{N}_4$  powders was shown in Fig. 3. The melamine powders were transformed into  $\text{g-C}_3\text{N}_4$  powders after a thermal polymerization reaction of  $550^\circ\text{C}$  for 5 h in a covered porcelain crucible. Moreover, the colors of the samples change from cream white color of melamine powders to light yellow color of  $\text{g-C}_3\text{N}_4$  powders, as shown in Fig. 3a and b. Seen from SEM images in Fig. 3c, the  $\text{g-C}_3\text{N}_4$  powders consist of numerous nanosheets with mixed lamellar and stacked structure. In particular, the micromorphology and size of the  $\text{g-C}_3\text{N}_4$  nanosheets are more uniform after ultrasonication, as shown in Fig. 3d.

During the preparation of  $\text{rGO/g-C}_3\text{N}_4/\text{Ag}$  NPs, an aqueous solution of glucose (5 wt%) was slowly added into a dispersion of  $\text{rGO/g-C}_3\text{N}_4$  and silver ammonia solution, and then  $[\text{Ag}(\text{NH}_3)_2]^+$  was reduced by the green reducing agent of glucose under  $70^\circ\text{C}$  water bath.

When the above hybrid mixture was remained static for 20 min, such that a bright silver mirror was attached onto the inside of the beaker, as shown in Fig. 4a. Interestingly, the ultrasonic treatment was instead of resting state,  $[\text{Ag}(\text{NH}_3)_2]^+$  was reduced not to form bright and uniform silver mirror, but to load into the  $\text{rGO/g-C}_3\text{N}_4$  nanocomposite as Ag NPs, as shown in Fig. 4b.

As a contrast, without the  $\text{rGO/g-C}_3\text{N}_4$  nanocomposite as a load carrier, the Ag NPs were prepared under  $70^\circ\text{C}$  water bath and ultrasonic treatment, and the microstructure of Ag NPs was analyzed by SEM and TEM. The obtained results show that the particle sizes of Ag NPs are 50–100 nm, as shown in Fig. 4c and d. In the formation process of Ag NPs without a carrier, the sizes of Ag NPs are not uniform, which may be attributed to some influencing factors such as agglomeration, surface coatings and overlapping.

Compared with  $\text{g-C}_3\text{N}_4$  sheets in Fig. 3d, the  $\text{rGO/g-C}_3\text{N}_4$  nanocomposite presents a 3D porous structure, which can effectively increase specific surface area and adsorption capacity, as shown in Fig. 5a and b. At the same time, the  $\text{rGO/g-C}_3\text{N}_4$  nanocomposite was successfully prepared in a high-pressure reactor at  $200^\circ\text{C}$  for 5 h, thus some oxygen-containing groups were removed from the GO surface.



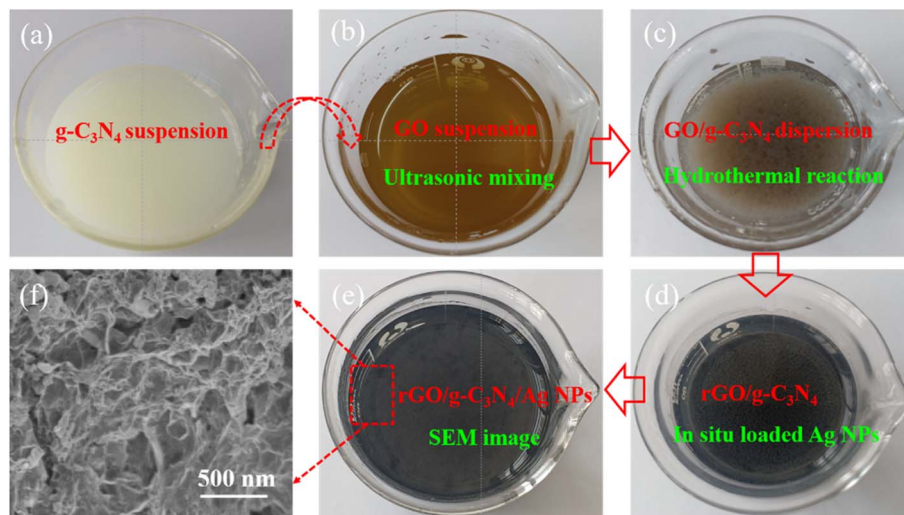


Fig. 1 A preparation schematic illustration of rGO/g-C<sub>3</sub>N<sub>4</sub>/Ag NPs. Optical photos of aqueous suspensions of g-C<sub>3</sub>N<sub>4</sub> (a), GO (b), GO/g-C<sub>3</sub>N<sub>4</sub> (c), rGO/g-C<sub>3</sub>N<sub>4</sub> (d), and rGO/g-C<sub>3</sub>N<sub>4</sub>/Ag NPs (e). SEM image of rGO/g-C<sub>3</sub>N<sub>4</sub>/Ag NPs (f).

Moreover, the electrical conductivity of rGO sheets will be greatly improved, as well as rGO and g-C<sub>3</sub>N<sub>4</sub> sheets are tightly bonded and their  $\pi$ - $\pi$  interactions has been strengthened, which are beneficial to promote the electron-hole separation.

As shown in Fig. 5c and d, the rGO/g-C<sub>3</sub>N<sub>4</sub>/Ag NPs has a 3D porous structure, while its microstructure can be further optimized, and numerous of Ag NPs are in loaded onto the surface or into inside of the nanocomposite.

Based on the above prepared GO, g-C<sub>3</sub>N<sub>4</sub> and rGO/g-C<sub>3</sub>N<sub>4</sub>, the rGO/g-C<sub>3</sub>N<sub>4</sub> loaded with Ag NPs was rationally constructed. Compared to g-C<sub>3</sub>N<sub>4</sub> sheets in Fig. 3d, the rGO/g-C<sub>3</sub>N<sub>4</sub> nanocomposite presents a 3D porous structure, which effectively

increases its specific surface area. Moreover, the hydrothermal reaction caused GO/g-C<sub>3</sub>N<sub>4</sub> to rGO/g-C<sub>3</sub>N<sub>4</sub>, and some oxygen-containing groups on GO surface were removed. Compared to rGO/g-C<sub>3</sub>N<sub>4</sub>, the rGO/g-C<sub>3</sub>N<sub>4</sub>/Ag NPs also presents a 3D porous structure, and its morphology can be further optimized due to *in situ* loading of Ag NPs, as shown in Fig. 5c and d.

To analyze the composition of rGO/g-C<sub>3</sub>N<sub>4</sub>/Ag NPs, its elemental mapping for elements (including C, O, N and Ag) was performed, as shown in Fig. 6. The elemental mappings of a selected region clearly demonstrate the corresponding distributions and atomic percents (C, O, N and Ag atoms).

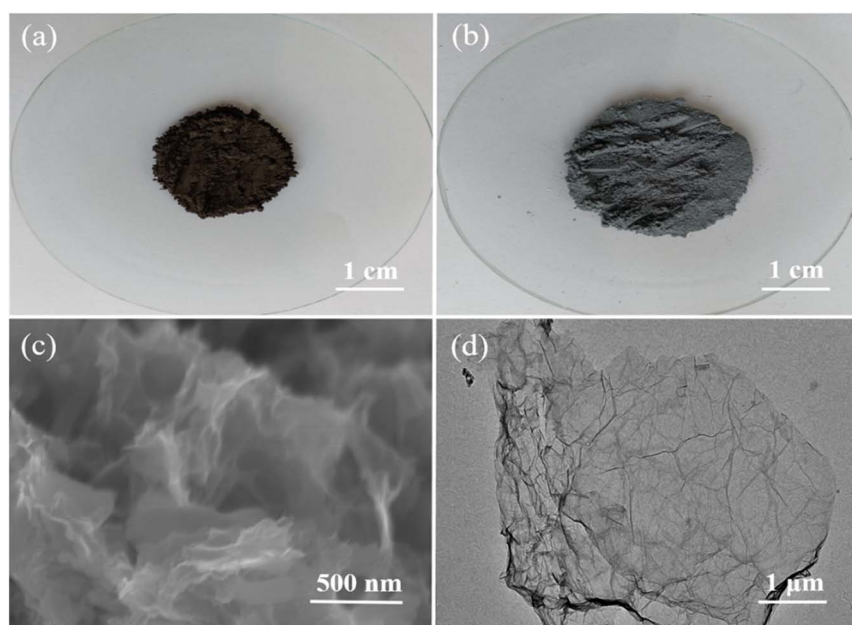


Fig. 2 Optical photos of graphite powders (a) and GO powders (b). SEM image of GO nanosheets (c) and TEM image of GO nanosheets (d).





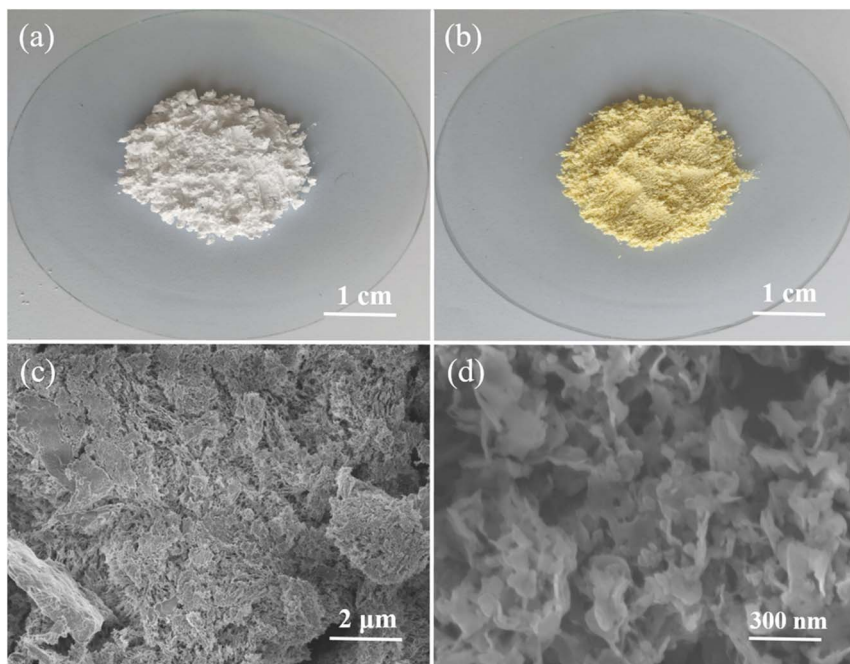


Fig. 3 Optical photos of melamine powders (a) and g-C<sub>3</sub>N<sub>4</sub> powders (b). SEM images of g-C<sub>3</sub>N<sub>4</sub> powders (c) and g-C<sub>3</sub>N<sub>4</sub> sheets (d).

As the same time, FTIR spectra are employed to analyze the functional groups of GO, g-C<sub>3</sub>N<sub>4</sub> and rGO/g-C<sub>3</sub>N<sub>4</sub>/Ag NPs. It can be seen from Fig. 7a that the characteristic peaks located at 3000–3500 cm<sup>−1</sup> should be caused by the stretching vibration of –OH and –NH<sub>2</sub> groups.<sup>56,57</sup> While the peaks of 1200–1700 cm<sup>−1</sup> are due to the stretching vibrations of CN heterocycles, and the peak of 806 cm<sup>−1</sup> is related to the breathing and stretching mode of CN-heterocyclic triazine. As mentioned above, the

characteristic peaks of FTIR spectra are completely consistent with the reported literature.<sup>56,57</sup>

The reaction temperature is considered as a crucial influencing factor on the crystallinity of g-C<sub>3</sub>N<sub>4</sub> sheets, which has played an important role on its photocatalytic activity.<sup>58</sup> Thus, different reaction temperatures (such as 500 °C, 550 °C and 600 °C) were considered based on the thermal polymerization reaction.<sup>52,58</sup> Compared with g-C<sub>3</sub>N<sub>4</sub> sheets prepared at 550 °C

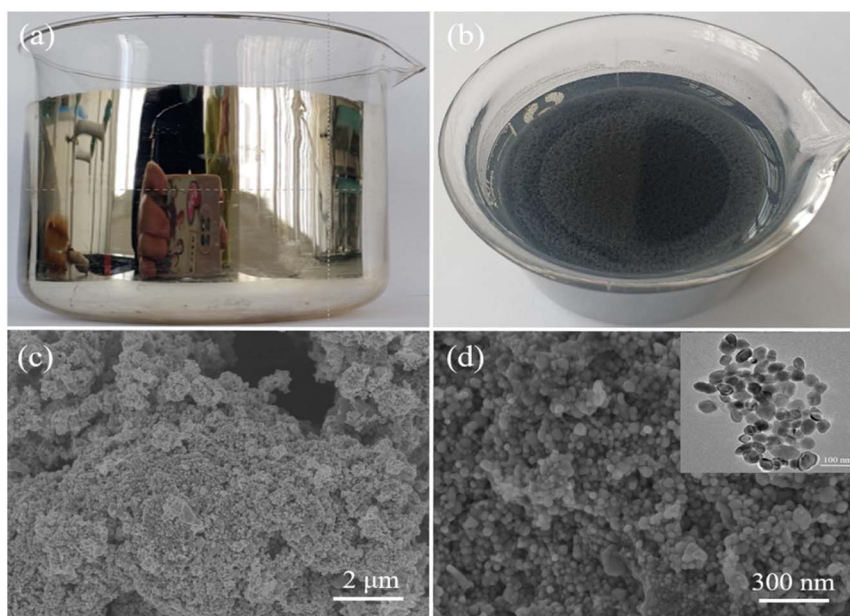


Fig. 4 Optical photos of silver mirror attached to the inside of a beaker (a) and rGO/g-C<sub>3</sub>N<sub>4</sub>/Ag NPs (b). SEM images of Ag NPs with different magnifications (c and d). The inset of (d) is TEM image of Ag NPs.

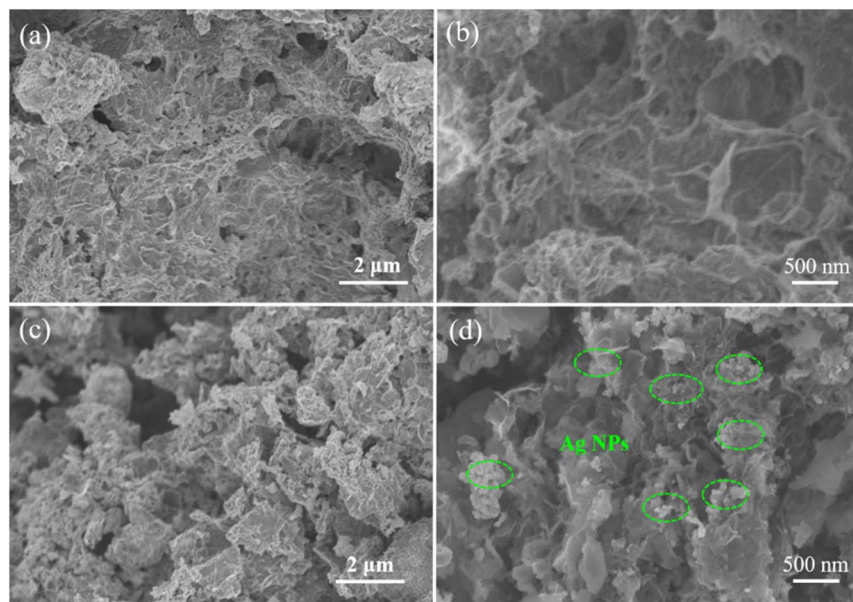


Fig. 5 SEM images of rGO/g-C<sub>3</sub>N<sub>4</sub> nanocomposite with different magnifications (a and b), and rGO/g-C<sub>3</sub>N<sub>4</sub>/Ag NPs with different magnifications (c and d).

and 600 °C, the characteristic FTIR peaks of g-C<sub>3</sub>N<sub>4</sub> sheets prepared at 500 °C are not obvious. Although the peak positions of g-C<sub>3</sub>N<sub>4</sub> sheets prepared at 550 °C and 600 °C are almost no difference, while there are obvious differences in their colors, that is, the color of g-C<sub>3</sub>N<sub>4</sub> sheets at 550 °C is light-yellow and the color of g-C<sub>3</sub>N<sub>4</sub> sheets at 600 °C is deep-yellow.

Seen from the characteristic FTIR peaks in Fig. 7b, the rGO/g-C<sub>3</sub>N<sub>4</sub>/Ag NPs contains some oxygen-containing functional groups. The absorption peak around 1600 cm<sup>-1</sup> is the basic skeleton of C=C bond, and the absorption peak near 1750 cm<sup>-1</sup> is the C=O stretching vibration absorption peak, as well as the absorption peak near 3400 cm<sup>-1</sup> is the O-H stretching vibration absorption peak.<sup>50,51</sup> Therefore, the rGO/g-C<sub>3</sub>N<sub>4</sub>/Ag NPs has some functional group structures, which will help it absorb pollutants from water for degradation.

Raman spectra in Fig. 8a show that the characteristic peak near 800 cm<sup>-1</sup> corresponds to the bending vibration of the triazine ring, and the characteristic peak near 1600 cm<sup>-1</sup> is

caused by the stretching vibration of the CN heterocyclic compound.<sup>59</sup> The Raman spectral characteristic peaks of g-C<sub>3</sub>N<sub>4</sub> prepared at 500 °C and 550 °C are more obvious compared with that of g-C<sub>3</sub>N<sub>4</sub> prepared at 600 °C. Based on above relevant analysis of FTIR and Raman spectra of g-C<sub>3</sub>N<sub>4</sub> samples prepared 500 °C, 550 °C and 600 °C, the g-C<sub>3</sub>N<sub>4</sub> powders in our experiment were deliberately prepared at 550 °C.<sup>52,58</sup>

It can be observed from Fig. 8b that the characteristic peaks near 1350 cm<sup>-1</sup> and 1600 cm<sup>-1</sup> correspond to the D and G bands of the graphite structure, respectively. Moreover, the ratio of D peak intensity to G peak intensity ( $I_D/I_G$ ) is generally used to represent the degree of graphitization of graphite,<sup>50</sup> after the hydrothermal reaction of rGO/g-C<sub>3</sub>N<sub>4</sub> and *in situ* loading of Ag NPs, the value of  $I_D/I_G$  increases from GO/g-C<sub>3</sub>N<sub>4</sub> and rGO/g-C<sub>3</sub>N<sub>4</sub> to rGO/g-C<sub>3</sub>N<sub>4</sub>/Ag NPs, indicating that some oxygen-containing groups in rGO/g-C<sub>3</sub>N<sub>4</sub> nanocomposite can be removed by heating reduction<sup>50</sup> and the Ag NPs have Raman enhancement effects.<sup>60</sup>

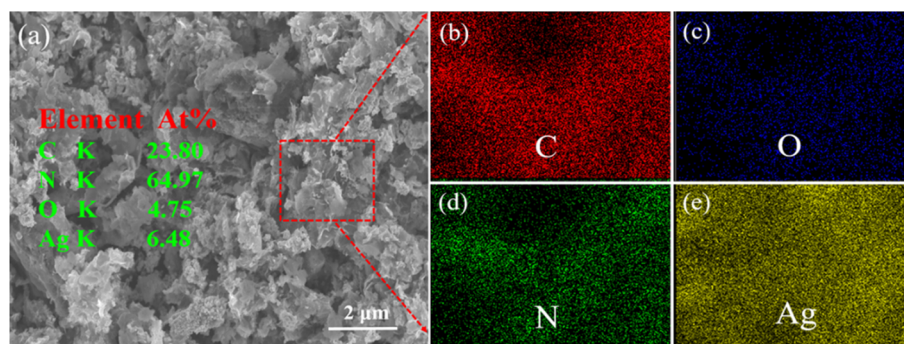


Fig. 6 (a) SEM image of rGO/g-C<sub>3</sub>N<sub>4</sub>/Ag NPs in a selected region, and (b–e) Elemental mappings of C, O, N and Ag.



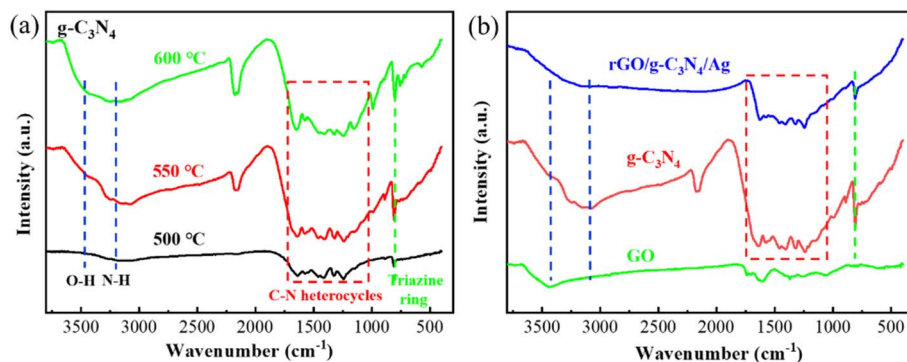


Fig. 7 FTIR spectra of g-C<sub>3</sub>N<sub>4</sub> sheets prepared at different temperatures (a), and FTIR spectra of GO, g-C<sub>3</sub>N<sub>4</sub> and rGO/g-C<sub>3</sub>N<sub>4</sub>/Ag NPs (b).

Seen from XRD analysis in Fig. 9a, there are a weak peak (13.2°) and a prominent peak (27.5°), which corresponds to the (100) and (002) crystal faces of g-C<sub>3</sub>N<sub>4</sub> sheet,<sup>52,56</sup> respectively. Moreover, the XRD patterns of g-C<sub>3</sub>N<sub>4</sub> sheets prepared at different temperatures (inset of Fig. 9a) show that the g-C<sub>3</sub>N<sub>4</sub> sheets prepared at 550 °C have more obvious characteristic peaks compared with that of g-C<sub>3</sub>N<sub>4</sub> sheets prepared at 500 °C and 600 °C.

For rGO sheets, the diffraction peak at 10.5° is a characteristic diffraction peak (Fig. 9b) of the crystal face of (001).<sup>50,51</sup> Especially, as displayed in Fig. 9c, the diffraction peaks of rGO/g-C<sub>3</sub>N<sub>4</sub> nanocomposite with Ag NPs located at 38.2° (111), 44.5° (200), 64.5° (220) and 77.5° (311) are the characteristic diffraction peaks of Ag NPs (JCPDS No. 04-0783),<sup>40,41</sup> respectively, indicating that Ag NPs were successfully introduced into the rGO/g-C<sub>3</sub>N<sub>4</sub> nanocomposite. The diffraction peaks of Ag NPs are strong and there are no other miscellaneous peaks, which confirms the high purity of Ag NPs.<sup>40,41</sup>

Very significantly, there is a noticeable change after *in situ* loading of Ag NPs, especially their intensity of the XRD patterns has changed in rGO/g-C<sub>3</sub>N<sub>4</sub>/Ag NPs. That is, a prominent peak at (002) and a weak peak at (100) crystal faces of g-C<sub>3</sub>N<sub>4</sub> sheets are shown in Fig. 9a, as well as a prominent peak at (002) crystal face of g-C<sub>3</sub>N<sub>4</sub> sheets and a weak peak at (001) crystal face of rGO sheets are shown in Fig. 9b. However, the diffraction peaks of Ag NPs are very strong, such that the diffraction peaks of g-C<sub>3</sub>N<sub>4</sub> sheets and rGO are too weak to be seen in rGO/g-C<sub>3</sub>N<sub>4</sub>/Ag NPs,

as shown in Fig. 9c. Moreover, the crystallite size of Ag NPs can play an important role on photocatalytic efficiency. Generally, smaller crystallites imply higher surface-to-volume ratio with enhancing photocatalytic activity.<sup>61</sup>

Thermogravimetric analysis was performed to calculate the water adsorption capacity of 3D porous structure.<sup>62</sup> As the adsorbed water evaporates at room temperature, the weight loss of this nanocomposite is about 56.7 wt%, and then the labile oxygen-containing functional groups are broken down to produce water at around 200 °C, the weight loss of hydrogel is about 20.7 wt%.<sup>63</sup>

### 3.2. Adsorption and catalytic properties

MB is generally employed as the model compound to detect the adsorption and catalytic properties of an adsorbent. The obtained rGO/g-C<sub>3</sub>N<sub>4</sub>/Ag NPs was used as an adsorbent and catalyst to remove MB from water. As control experiments, the pristine g-C<sub>3</sub>N<sub>4</sub> sheets and rGO/g-C<sub>3</sub>N<sub>4</sub> nanocomposite were also employed as adsorbents and catalysts to remove MB from water under the same experimental conditions, respectively.

Firstly, the test experiments were carried out under alkaline medium, that is, the pH value of an aqueous solution containing MB was about 8.<sup>28</sup> Typically, 100 mg of adsorbent (such as g-C<sub>3</sub>N<sub>4</sub> sheets, rGO/g-C<sub>3</sub>N<sub>4</sub> and rGO/g-C<sub>3</sub>N<sub>4</sub>/Ag NPs) was immersed into 100 mL of MB solution (50 mg L<sup>-1</sup>) in the dark, followed by stirring at 200 rpm at room temperature. At time

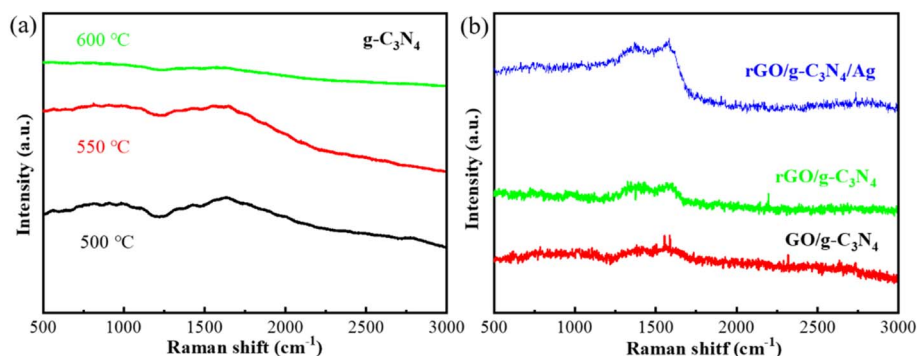


Fig. 8 Raman spectra of g-C<sub>3</sub>N<sub>4</sub> sheets prepared at different temperatures (a), and GO/g-C<sub>3</sub>N<sub>4</sub>, rGO/g-C<sub>3</sub>N<sub>4</sub> and rGO/g-C<sub>3</sub>N<sub>4</sub>/Ag NPs (b).





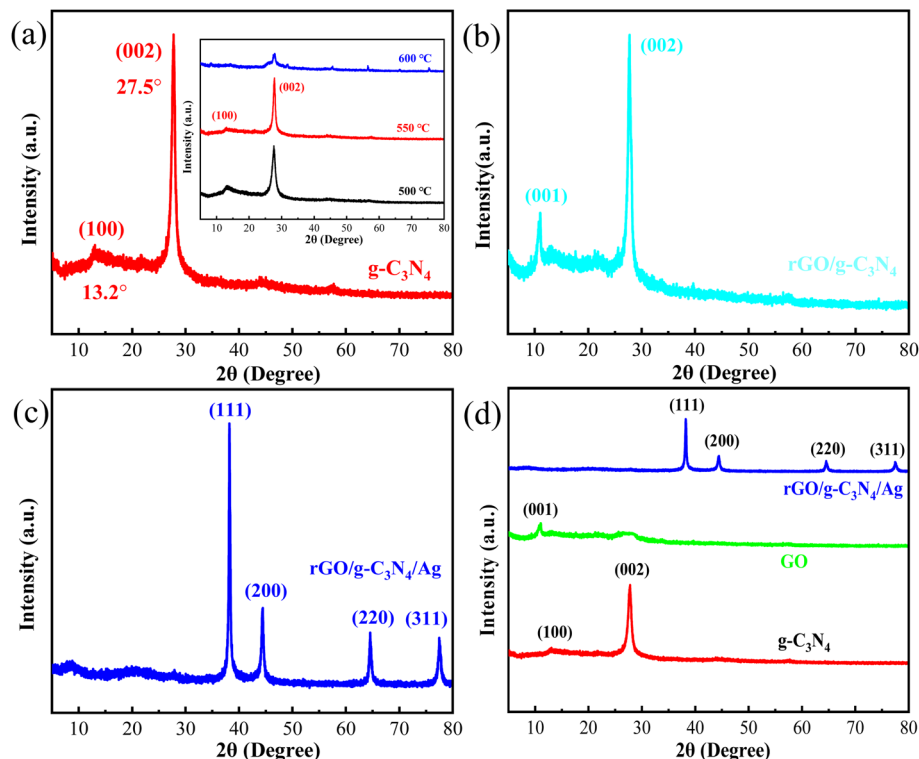


Fig. 9 XRD patterns of (a) g-C<sub>3</sub>N<sub>4</sub> sheets prepared at 550 °C, (b) rGO/g-C<sub>3</sub>N<sub>4</sub>, (c) rGO/g-C<sub>3</sub>N<sub>4</sub>/Ag NPs and (d) g-C<sub>3</sub>N<sub>4</sub>, GO and rGO/g-C<sub>3</sub>N<sub>4</sub>/Ag NPs. The inset of (a) is XRD patterns of g-C<sub>3</sub>N<sub>4</sub> sheets prepared at different temperatures.

intervals of 10 min, the adsorbent was separated by filtration and the concentration of residual MB in the filtrate was calculated by Beer's law based on the absorption peak at 662 nm with a UV-visible spectrophotometer (Shimadzu UV-2450).<sup>51,63–65</sup>

Secondly, under simulated solar irradiation, a light resource was introduced using a 300 W Xe lamp. Typically, 100 mg of adsorbent was immersed into 100 mL of MB solution (50 mg L<sup>-1</sup>) under simulated solar irradiation, followed by stirring at 200 rpm at room temperature. At time intervals of 10 min, the adsorbent was separated by filtration and the concentration of residual MB in the filtrate was calculated by Beer's law based on the absorption peak at 662 nm with a UV-visible spectrophotometer (Shimadzu UV-2450).<sup>51,63–65</sup>

Finally, the ratio of temporal concentration to initial concentration ( $C/C_0$ ) was analyzed with the change of adsorption time. The elimination efficiency was assessed by using  $C/C_0$ , which is equal to  $A/A_0$ . Where  $A_0$  and  $C_0$  were the initial absorbance and concentration of MB, respectively. The  $A$  and  $C$  were the corresponding absorbance and concentration of MB to be tested at different adsorption times, respectively.

As can be seen from Fig. 10a, when the pristine g-C<sub>3</sub>N<sub>4</sub> sheets acts as an adsorbent to adsorb MB from water in the dark, it takes about 60 min to reach adsorption equilibrium and the value of  $C/C_0$  decreases to 21.80%. Moreover, the rGO/g-C<sub>3</sub>N<sub>4</sub> nanocomposite acts as an adsorbent, the adsorption reaches equilibrium at 60 min and the value of  $C/C_0$  decreases to 15.80%. While the rGO/g-C<sub>3</sub>N<sub>4</sub>/Ag NPs is used as the adsorbent,

the adsorption equilibrium time is also 60 min and the value of  $C/C_0$  decreases to 12.80%.

As a control experiment, the visible light was introduced on the basis of the above same experimental conditions, the pristine g-C<sub>3</sub>N<sub>4</sub> sheets, rGO/g-C<sub>3</sub>N<sub>4</sub> and rGO/g-C<sub>3</sub>N<sub>4</sub>/Ag NPs were employed as adsorbents and catalysts, respectively. At equilibrium, their values of  $C/C_0$  decrease to 18.80%, 10.80% and 0.80%, respectively, as shown in Fig. 10b.

From the above results, it was reasoned that the pristine g-C<sub>3</sub>N<sub>4</sub> sheets, rGO/g-C<sub>3</sub>N<sub>4</sub> and rGO/g-C<sub>3</sub>N<sub>4</sub>/Ag NPs were only employed as adsorbents in the dark, respectively, and their removal capacities (Fig. 10c) were calculated as 39.10 mg g<sup>-1</sup>, 42.10 mg g<sup>-1</sup>, and 43.60 mg g<sup>-1</sup>, respectively. However, as the visible light is introduced, they are not only adsorbents but also catalysts, such that there is a significant decline in their values of  $C/C_0$  (from 21.80%, 15.80% and 12.80% to 18.80%, 10.80% and 0.80%), as well as their removal capacities (Fig. 10d) are up to 40.60 mg g<sup>-1</sup>, 44.70 mg g<sup>-1</sup>, and 49.60 mg g<sup>-1</sup>, respectively. Compared with the pristine g-C<sub>3</sub>N<sub>4</sub> sheets and rGO/g-C<sub>3</sub>N<sub>4</sub>, the rGO/g-C<sub>3</sub>N<sub>4</sub>/Ag NPs has best performance.

Among them, a 3D porous structure of rGO/g-C<sub>3</sub>N<sub>4</sub> nanosheets with rich functional groups provides an effective carrier to hybridize with Ag NPs and adsorb MB, as well as enhance light absorption.<sup>39</sup> The rGO nanosheets act as the charge transmission bridge between g-C<sub>3</sub>N<sub>4</sub> nanosheets and Ag NPs, which not only facilitates the separation of electrons and holes but also improves the stability of the photocatalyst of Ag NPs.<sup>37,39</sup> The Ag NPs can display a plasmon effect of the localized





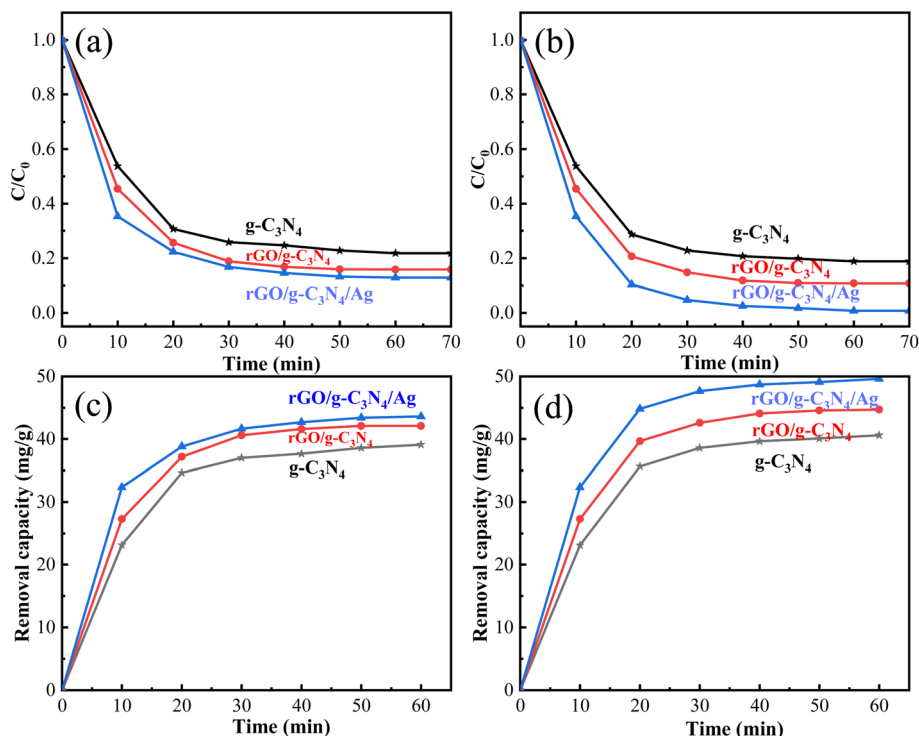


Fig. 10 The ratio of temporal concentration to initial concentration ( $C/C_0$ ) with the change of adsorption time (a) in the dark and (b) under visible light. MB removal capacity with the change of adsorption time (c) in the dark and (d) under visible light.

surface plasmon resonance, such that the Ag NPs not only act as photocatalyst, but also enhance light absorption and promote charge separation.<sup>40–45,60</sup>

Based on the above analysis, the rGO/g-C<sub>3</sub>N<sub>4</sub>/Ag NPs was employed as not only adsorbent but also catalyst under visible light irradiation, and their values of  $C/C_0$  decrease from 12.80% to 0.80%, with MB removal capacity increase from 43.60 mg g<sup>-1</sup> to 49.60 mg g<sup>-1</sup>. Under visible light irradiation, the adsorption and catalytic performance of rGO/g-C<sub>3</sub>N<sub>4</sub>/Ag NPs is better than that reported in many literature, which is compared with the related reports,<sup>51,53,63,64,66,67</sup> as shown in Table 1.

The pH of the system is a very important factor, which influences the photocatalytic degradation activities of the catalysts.<sup>28,68</sup> Fig. 11a demonstrates the performance of this catalyst of rGO/g-C<sub>3</sub>N<sub>4</sub>/Ag NPs at different pH values towards the degradation of MB. There is a basic tendency to increase

catalytic activity as pH increases, reaching a maximum value at pH value of 11.<sup>69</sup>

In our experiment, MB is selected as a model compound that is a cationic dye. Although the pH of the system is a very important factor, at the same time, positively charged ions with strong electrostatic interactions will interfere with the efficiency of the method. Moreover, if some ions get through  $\pi$ - $\pi$  interactions to compete for active sites on surface of catalyst, they can also interfere with the efficiency of this method.

The stability and reusability of a catalyst is very important for assessing the practical applicability of the catalyst. After a run, the filtered photocatalyst was washed for three times with ethanol and deionized water, respectively, and dried at 80 °C for 5 h. After 4 cycles, the efficiency of this photocatalyst is still more than 90%, as shown in Fig. 11b.

### 3.3. Analysis of catalytic process and mechanism

In our experiments, a possible mechanism was proposed to explain photocatalytic degradation of MB under visible light irradiation. The evaluations of various reactive species were done to confirm their contribution towards MB degradation. Several chemical agents were selected as quenchers,<sup>62,68,70</sup> such as ethylenediaminetetraacetic acid disodium (EDTA-2Na) for holes ( $h^+$ ), methanol for hydroxyl radicals ( $\cdot OH$ ) and benzoquinone for superoxide ( $\cdot O_2^-$ ), respectively. The production of  $\cdot O_2^-$  radicals was confirmed as the most dominant radicals that can lead to enhanced photocatalytic degradation of MB on the catalyst surface. Moreover, the *in situ* loaded Ag NPs

Table 1 Adsorbents or catalysts for removal of MB

Adsorbents or catalyst	Pollutants	Removal capacity (mg g <sup>-1</sup> )	Ref.
N-RGO	MB	94.4	63
rGO/g-C <sub>3</sub> N <sub>4</sub> /Ag	MB	49.60	This work
g-C <sub>3</sub> N <sub>4</sub> /GO	MB	30.0	53
Biomass activated carbon	MB	24.0	64
GO	MB	23.8	51
GO/polyaniline	MB	6.70	66
TiO <sub>2</sub> /GO composites	MB	5.01	67



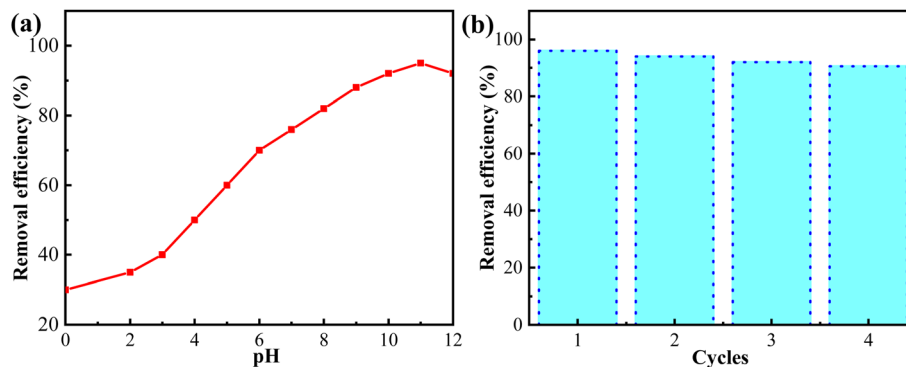


Fig. 11 Photocatalytic degradation of MB under visible light irradiation. (a) Effect of solution pH and (b) stability experiments for MB degradation.

synergistically increase the generation of reactive oxygen species proposed to be  $\cdot\text{O}_2^-$  through redox reactions.

There are three kinds of heterojunctions existing in rGO/g-C<sub>3</sub>N<sub>4</sub>/Ag NPs, that is, the heterojunctions exist between rGO/g-C<sub>3</sub>N<sub>4</sub>, g-C<sub>3</sub>N<sub>4</sub>/Ag and rGO/Ag, and they will play relevant roles in the photocatalytic process. As a typical n-type semiconductor, the g-C<sub>3</sub>N<sub>4</sub> nanosheet can be excited to generate photo-generated electrons and holes under visible light irradiation. In this 3D rGO/g-C<sub>3</sub>N<sub>4</sub>/Ag NPs, rGO is not only used to enhance light absorption, but also used as an excellent conductor of electrons to promote the separation of photogenerated electron-hole pairs.<sup>53</sup> At the same time, Ag NPs has a strong localized surface plasmon resonance effect under visible light irradiation, which not only enhances light absorption, but also increases the generation rate of photogenerated electron-hole pairs on the surface of g-C<sub>3</sub>N<sub>4</sub>.<sup>40,41,44,45,54</sup> In the 3D network structure, rGO, g-C<sub>3</sub>N<sub>4</sub> and Ag NPs play an effective synergistic role to overcome the drawbacks of g-C<sub>3</sub>N<sub>4</sub>-based photocatalyst such as small specific surface area, fast charge recombination and limited visible-light absorption. Thus the photogenerated electrons generated by g-C<sub>3</sub>N<sub>4</sub> nanosheet under the excitation of visible light can effectually react with O<sub>2</sub> to form the active species  $\cdot\text{O}_2^-$  to catalyze the decomposition of MB.

Based on the above photocatalytic analysis and the mechanism proposed, the kinetic of adsorption and degradation of MB belongs to pseudo-first order kinetics.<sup>34,54,68</sup> Under visible light irradiation, the reaction rate constants of g-C<sub>3</sub>N<sub>4</sub> sheets and rGO/g-C<sub>3</sub>N<sub>4</sub> were calculated as 0.02622/min and 0.03608/min, respectively. While the reaction rate constant of rGO/g-C<sub>3</sub>N<sub>4</sub>/Ag NPs was calculated as 0.07795/min, which is higher than that g-C<sub>3</sub>N<sub>4</sub> sheets and rGO/g-C<sub>3</sub>N<sub>4</sub>.

## 4. Conclusion

In conclusion, we developed a facile step-by-step approach (including ultrasonic mixing, hydrothermal reaction and *in situ* loading) to fabricate a 3D rGO/g-C<sub>3</sub>N<sub>4</sub> nanocomposite loaded with Ag NPs. Due to the synergistic effect of rGO, g-C<sub>3</sub>N<sub>4</sub> and Ag NPs, this obtained nanocomposite with excellent performance can be used as adsorbent and catalyst to efficiently remove MB (50 mg L<sup>-1</sup>) from water under visible light, and its MB removal

capacity is high as 49.60 mg g<sup>-1</sup> within 60 min. This work provides a useful reference for the rational design and scale preparation of rGO/g-C<sub>3</sub>N<sub>4</sub> nanocomposites for practical applications.

## Data availability

The authors declare that the raw data supporting this article are available from the corresponding author upon reasonable request.

## Author contributions

Kesheng Cao, and Xueyu Ge: conceptualization, methodology, and writing original draft; Shuang Li, Suyu Cui, Guijin Guo, and Liuqing Yang: investigation, validation, and data analysis; Xingwu Li, Yabo Wang, and Suzhen Bai: data analysis, review, and editing; Zhengshan Tian, Qian Wei, and Wei Li: writing, review, editing, and supervision.

## Conflicts of interest

The authors declare no conflict of interest.

## Acknowledgements

This work was supported by the Henan Province science and technology research project (242102230037 and 252102231024) and Henan Province Science and Technology Research and Development Plan Joint Fund (Industry Category) Key Project "Key Technologies and Applications of High-Performance Para-Aramid Fiber for Insulation Tie Rod".

## References

- 1 G. Bayramoglu, B. Altintas and M. Y. Arica, Adsorption kinetics and thermodynamic parameters of cationic dyes from aqueous solutions by using a new strong cation-exchange resin, *Chem. Eng. J.*, 2009, **152**, 339–346.
- 2 H. P. Mota, R. F. Quadrado, B. A. Iglesias and A. R. Fajardo, Enhanced photocatalytic degradation of organic pollutants



- mediated by Zn (II)-porphyrin/poly (acrylic acid) hybrid microparticles, *Appl. Catal., B*, 2020, **277**, 119208.
- 3 A. L. T. Zheng, S. Boonyuen and Y. Andou, Porous graphene-based materials for enhanced adsorption towards emerging micropollutants (EMs), in *Handbook of Porous Carbon Materials. Materials Horizons: from Nature to Nanomaterials*, ed. A. N. Grace, P. Sonar, P. Bhardwaj and A. Chakravorty, Springer, Singapore, 2023, pp. 547–570.
  - 4 H. Naeem, M. Ajmal, R. B. Qureshi, S. T. Muntha, M. Farooq and M. Siddiq, Facile synthesis of graphene oxide–silver nanocomposite for decontamination of water from multiple pollutants by adsorption, catalysis and antibacterial activity, *J. Environ. Manage.*, 2019, **230**, 199–211.
  - 5 W. Pu, Y. Zhou, L. Yang, H. Gong, Y. Li, Q. Yang and D. Zhang, High-efficiency crystalline carbon nitride photocatalysts: status and perspectives, *Nano Res.*, 2024, **17**(9), 7840–7863.
  - 6 H. Li, B. Cheng, J. Xu, J. Yu and S. Cao, Crystalline carbon nitrides for photocatalysis, *EES Catal.*, 2024, **2**, 411–447.
  - 7 S. Hou, X. Gao, X. Lv, Y. Zhao, X. Yin, Y. Liu, J. Fang, X. Yu, X. Ma, T. Ma and D. Su, Decade milestone advancement of defect-engineered g-C<sub>3</sub>N<sub>4</sub> for solar catalytic applications, *Nano-Micro Lett.*, 2024, **16**, 70.
  - 8 A. K. Geim, Graphene: status and prospects, *Science*, 2009, **324**, 1530–1534.
  - 9 A. K. Geim and K. S. Novoselov, The rise of graphene, *Nat. Mater.*, 2007, **6**, 183–191.
  - 10 X. Li, J. Yu, S. Wageh, A. A. Al-Ghamdi and J. Xie, Graphene in photocatalysis: a review, *Small*, 2016, **12**, 6640–6696.
  - 11 Q. Xiang, J. Yu and M. Jaroniec, Graphene-based semiconductor photocatalysts, *Chem. Soc. Rev.*, 2012, **41**, 782–796.
  - 12 X. Fan, G. Zhang and F. Zhang, Multiple roles of graphene in heterogeneous catalysis, *Chem. Soc. Rev.*, 2015, **44**, 3023–3035.
  - 13 C.-L. Chen and Q.-W. Chen, Doped graphene for metal-free catalysis, *Chem. Soc. Rev.*, 2014, **43**, 2841–2857.
  - 14 M. D. F. Hossain, N. Akther and Y. Zhou, Recent advancements in graphene adsorbents for wastewater treatment: current status and challenges, *Chin. Chem. Lett.*, 2020, **31**, 2525–2538.
  - 15 J. H. Lee, A. Avsar, J. Jung, J. Y. Tan, K. Watanabe, T. Taniguchi, S. Natarajan, G. Eda, S. Adam, A. H. Castro Neto and B. Özyilmaz, Van der Waals force: a dominant factor for reactivity of graphene, *Nano Lett.*, 2015, **15**, 319–325.
  - 16 S. Tsoi, P. Dev, A. L. Friedman, R. Stine, J. T. Robinson, T. L. Reinecke and P. E. Sheehan, Van der Waals screening by single-layer graphene and molybdenum disulfide, *ACS Nano*, 2014, **8**, 12410–12417.
  - 17 D. R. Dreyer, A. D. Todd and C. W. Bielawski, Harnessing the chemistry of graphene oxide, *Chem. Soc. Rev.*, 2014, **43**, 5288–5301.
  - 18 D. C. Marcano, D. V. Kosynkin, J. M. Berlin, A. Sinitskii, Z. Sun, A. Slesarev, L. B. Alemany, W. Lu and J. M. Tour, Improved synthesis of graphene oxide, *ACS Nano*, 2010, **4**, 4806–4814.
  - 19 A. M. Dimiev and J. M. Tour, Mechanism of graphene oxide formation, *ACS Nano*, 2014, **8**, 3060–3068.
  - 20 S. J. Wu, N. Duan, Y. T. Qiu, J. H. Li and Z. P. Wang, Colorimetric aptasensor for the detection of *Salmonella enterica* serovar typhimurium using ZnFe<sub>2</sub>O<sub>4</sub>-reduced graphene oxide nanostructures as an effective peroxidase mimetics, *Int. J. Food Microbiol.*, 2017, **261**, 42–48.
  - 21 Y. W. Xu, W. Zhang, J. Y. Shi, X. B. Zou, Y. X. Li, H. E. Tahir, X. W. Huang, Z. H. Li, X. D. Zhai and X. T. Hu, Electrodeposition of gold nanoparticles and reduced graphene oxide on an electrode for fast and sensitive determination of methylmercury in fish, *Food Chem.*, 2017, **237**, 423–430.
  - 22 C. Su and K. P. Loh, Carbocatalysts: graphene oxide and its derivatives, *Acc. Chem. Res.*, 2013, **46**, 2275–2285.
  - 23 H. Liu and H. Qiu, Recent advances of 3D graphene-based adsorbents for sample preparation of water pollutants: A review, *Chem. Eng. J.*, 2020, **393**, 124691.
  - 24 Y. Zhu, S. Murali, W. Cai, X. Li, J. W. Suk, J. R. Potts and R. S. Ruoff, Graphene and graphene oxide: synthesis, properties, and applications, *Adv. Mater.*, 2010, **22**, 3906–3924.
  - 25 W. S. Zhou, C. H. Li, C. Sun and X. D. Yang, Simultaneously determination of trace Cd<sup>2+</sup> and Pb<sup>2+</sup> based on L-cysteine/graphene modified glassy carbon electrode, *Food Chem.*, 2016, **192**, 351–357.
  - 26 X. W. Han, S. Guo, T. Li, J. Peng and H. Pan, Construction of Ag/3D-reduced graphene oxide nanocomposite with advanced catalytic capacity for 4-nitrophenol and methylene blue, *Colloid. Surface. A.*, 2022, **650**, 128688.
  - 27 N. M. Dat, P. N. B. Long, D. C. U. Nhi, N. N. Minh, H. M. Nam, M. T. Phong and N. H. Hieu, Synthesis of silver/reduced graphene oxide for antibacterial activity and catalytic reduction of organic dyes, *Synth. Met.*, 2020, **260**, 116260.
  - 28 J. Rath, J. K. Sahoo, S. K. Sahoo, B. Komali, R. R. Meher, S. Madhuri and S. K. Biswal, Green synthesis of silver nanoparticles decorated on graphene oxide for crystal violet dye removal, *Diam. Relat. Mater.*, 2024, **146**, 111192.
  - 29 H. G. Mohamed, A. Nour, A. I. Abd-Elhamid, *et al*, Enhancement of methylene blue catalytic reduction by novel green synthesized metal decorated reduced graphene oxide: Sn@rGO and Ag@rGO, *J. Alloy. Compd.*, 2024, **997**, 174920.
  - 30 X. Wang, K. Maeda, A. Thomas, *et al*, A metal-free polymeric photocatalyst for hydrogen production from water under visible light, *Nat. Mater.*, 2009, **8**, 76–80.
  - 31 W. J. Ong, L. L. Tan, Y. H. Ng, S. T. Yong and S. P. Chai, Graphitic carbon nitride (g-C<sub>3</sub>N<sub>4</sub>)-based photocatalysts for artificial photosynthesis and environmental remediation: are we a step closer to achieving sustainability?, *Chem. Rev.*, 2016, **116**, 7159–7329.
  - 32 Y. Li, M. Zhou, B. Cheng and Y. Shao, Recent advances in g-C<sub>3</sub>N<sub>4</sub>-based heterojunction photocatalysts, *J. Mater. Sci. Technol.*, 2020, **56**, 1–17.
  - 33 J. Xiao, Y. Xie, J. Rabeah, A. Bruckner and H. Cao, Visible-light photocatalytic ozonation using graphitic C<sub>3</sub>N<sub>4</sub>





- catalysts: a hydroxyl radical manufacturer for wastewater treatment, *Acc. Chem. Res.*, 2020, **53**, 1024–1033.
- 34 A. F. Pérez-Torres, *et al*, Sulfur-doped g-C<sub>3</sub>N<sub>4</sub> heterojunctions for efficient visible light degradation of methylene blue, *ACS Omega*, 2023, **8**, 47821–47834.
  - 35 Y. Li, M. Gu, X. Zhang, J. Fan, K. Lv, S. A. C. Carabineiro and F. Dong, 2D g-C<sub>3</sub>N<sub>4</sub> for advancement of photogenerated carrier dynamics: status and challenges, *Mater. Today*, 2020, **41**, 270–303.
  - 36 M. Chen, M. Sun, X. Cao, *et al*, Progress in preparation, identification and photocatalytic application of defective g-C<sub>3</sub>N<sub>4</sub>, *Coordin. Chem. Rev.*, 2024, **510**, 215849.
  - 37 W. Li, X. Chu, F. Wang, Y. Dang, X. Liu, X. Wang and C. Wang, Enhanced cocatalyst-support interaction and promoted electron transfer of 3D porous g-C<sub>3</sub>N<sub>4</sub>/GO-M (Au, Pd, Pt) composite catalysts for hydrogen evolution, *Appl. Catal. B: Environ.*, 2021, **288**, 120034.
  - 38 A. L. T. Zheng, T. Ohno and Y. Andou, Recent progress in photocatalytic efficiency of hybrid three-dimensional (3D) graphene architectures for pollution remediation, *Top. Catal.*, 2022, **65**, 1634–1647.
  - 39 S. Patnaik, A. Behera and K. Parida, A review on g-C<sub>3</sub>N<sub>4</sub>/graphene nanocomposites: multifunctional roles of graphene in the nanohybrid photocatalyst toward photocatalytic applications, *Catal. Sci. Technol.*, 2021, **11**, 6018–6040.
  - 40 X. Jiang, L. Zhang, H. Liu, D. Wu, F. Wu, L. Tian, L. Liu, J. Zou, S. Luo and B. Chen, Silver single atom in carbon nitride catalyst for highly efficient photocatalytic hydrogen evolution, *Angew. Chem., Int. Ed.*, 2020, **59**, 23112–23116.
  - 41 F. Chen, H. Yang, W. Luo, P. Wang, H. Yu and G. Selective, adsorption of thiocyanate anions on Ag-modified g-C<sub>3</sub>N<sub>4</sub> for enhanced photocatalytic hydrogen evolution, *Chin. J. Catal.*, 2017, **38**, 1990–1998.
  - 42 W. Liu, W. Hu, L. Yang and J. Liu, Single cobalt atom anchored on carbon nitride with well-defined active sites for photo-enzyme catalysis, *Nano Energy*, 2020, **73**, 104750.
  - 43 Z. Zeng, Y. Su, X. Quan, W. Choi, G. Zhang, N. Liu, B. Kim, S. Chen, H. Yu and S. Zhang, Single-atom platinum confined by the interlayer nanospace of carbon nitride for efficient photocatalytic hydrogen evolution, *Nano Energy*, 2020, **69**, 104409.
  - 44 Z. Chen, S. Pronkin, T. P. Feller, *et al*, Merging single-atom-dispersed silver and carbon nitride to a joint electronic system via copolymerization with silver tricyanomethanide, *ACS Nano*, 2016, **10**, 3166–3175.
  - 45 L. Sun, Y. Feng, K. Ma, X. Jiang, Z. Gao, J. Wang, N. Jiang and X. Liu, Synergistic effect of single-atom Ag and hierarchical tremella-like g-C<sub>3</sub>N<sub>4</sub>: electronic structure regulation and multi-channel carriers transport for boosting photocatalytic performance, *Appl. Catal. B: Environ.*, 2022, **306**, 121106.
  - 46 J. Fu, J. Yu, C. Jiang and B. Cheng, g-C<sub>3</sub>N<sub>4</sub>-based heterostructured photocatalysts, *Adv. Energy Mater.*, 2018, **8**(3), 1701503.
  - 47 Y. Luo, Y. Zhu, Y. Han, *et al*, g-C<sub>3</sub>N<sub>4</sub>-based photocatalysts for organic pollutant removal: a critical review, *Carbon Res.*, 2023, **2**, 14.
  - 48 W. S. Hummers and R. E. Offeman, Preparation of graphitic oxide, *J. Am. Chem. Soc.*, 1958, **80**, 1339.
  - 49 C. C. Qin, W. L. Guo, Y. Liu, Z. C. Liu, J. Qiu and J. B. Peng, A Novel electrochemical sensor based on graphene oxide decorated with silver nanoparticles-molecular imprinted polymers for determination of Sunset Yellow in soft drinks, *Food. Anal. Method.*, 2017, **10**(7), 2293–2301.
  - 50 Z. Tian, J. Li, G. Zhu, J. Lu, Y. Wang, Z. Shi and C. Xu, Facile synthesis of highly conductive sulfur-doped reduced graphene oxide sheets, *Phys. Chem. Chem. Phys.*, 2016, **18**, 1125–1130.
  - 51 K. Cao, Z. Tian, X. Zhang, Y. Wang and Q. Zhu, Green preparation of graphene oxide nanosheets as adsorbent, *Sci. Rep.*, 2023, **13**, 9314.
  - 52 F. Yang, D. Liu, Y. Li, L. Cheng and J. Ye, Salt-template-assisted construction of honeycomb-like structured g-C<sub>3</sub>N<sub>4</sub> with tunable band structure for enhanced photocatalytic H<sub>2</sub> production, *Appl. Catal. B: Environ.*, 2019, **240**, 64–71.
  - 53 L. Tang, C. T. Jia, Y. C. Xue, L. Li, A. Q. Qang, G. Xu, N. Liu and M. H. Wu, Fabrication of compressible and recyclable macroscopic g-C<sub>3</sub>N<sub>4</sub>/GO aerogel hybrids for visible light harvesting: A promising strategy for water remediation, *Appl. Catal. B.*, 2017, **219**, 241–248.
  - 54 Y. Song, Y. Peng, N. V. Long, Z. Huang and Y. Yang, Multifunctional self-assembly 3D Ag/g-C<sub>3</sub>N<sub>4</sub>/RGO aerogel as highly efficient adsorbent and photocatalyst for R6G removal from wastewater, *Appl. Surf. Sci.*, 2021, **542**, 148584.
  - 55 X. Xu, Q. Q. Zhang, Y. K. Yu, W. L. Chen, H. Hu and H. Li, Naturally dried graphene aerogels with superelasticity and tunable Poisson's ratio, *Adv. Mater.*, 2016, **28**, 9223–9230.
  - 56 F. He, Y. Lu, Y. Wu, *et al*, Rejoice of carbon nitride fragments into multi-interfacial order-disorder homojunction for robust photo-driven generation of H<sub>2</sub>O<sub>2</sub>, *Adv. Mater.*, 2024, **36**, 2307490.
  - 57 D. Zhao, C. L. Dong, B. Wang, *et al*, Synergy of dopants and defects in graphitic carbon nitride with exceptionally modulated band structures for efficient photocatalytic oxygen evolution, *Adv. Mater.*, 2019, **31**, 1903545.
  - 58 S. Cao, J. Low, J. Yu and M. Jaroniec, Polymeric photocatalysts based on graphitic carbon nitride, *Adv. Mater.*, 2015, **27**, 2150–2176.
  - 59 Y. Zhang, J. Wu, Y. Deng, Y. Xin, H. Liu, D. Ma and N. Bao, Synthesis and visible-light photocatalytic property of Ag/GO/g-C<sub>3</sub>N<sub>4</sub> ternary composite, *Mater. Sci. Eng. B*, 2017, **221**, 1–9.
  - 60 L. Zhao, C. Deng, S. Xue, H. Liu, L. Hao and M. Zhu, Multifunctional g-C<sub>3</sub>N<sub>4</sub>/Ag NPs intercalated GO composite membrane for SERS detection and photocatalytic degradation of paraoxon-ethyl, *Chem. Eng. J.*, 2020, **402**, 126223.
  - 61 V. Kathiravan, Green synthesis of silver nanoparticles using different volumes of *Trichodesma indicum* leaf extract and their antibacterial and photocatalytic activities, *Res. Chem. Intermed.*, 2018, **44**, 4999–5012.



- 62 M. VafaeiAsl, P. Jamshidi, F. Shemirani, *et al*, Immobilizing nanocatalyst onto polyvinyl alcohol cross-linked by sodium alginate: a new strategy to degrade high amount of chloramphenicol and amitriptyline, *Res. Chem. Intermed.*, 2024, **50**, 4721–4744.
- 63 Z. Tian, *et al*, One-pot hydrothermal synthesis of nitrogen-doped reduced graphene oxide hydrogel, *Sci. Adv. Mater.*, 2015, **7**, 1415–1423.
- 64 S. Bai, T. Wang, Z. Tian, K. Cao and J. Li, Facile preparation of porous biomass charcoal from peanut shell as adsorbent, *Sci. Rep.*, 2020, **10**, 15845.
- 65 H. Moussa, *et al*, ZnO rods/reduced graphene oxide composites prepared *via* a solvothermal reaction for efficient sunlight-driven photocatalysis, *Appl. Catal. B Environ.*, 2016, **185**, 11–21.
- 66 E. A. El-Sharkaway, *et al*, Removal of methylene blue from aqueous solutions using polyaniline/graphene oxide or polyaniline/reduced graphene oxide composites, *Environ. Technol.*, 2020, **41**, 2854–2862.
- 67 T. D. Nguyen-Phan, *et al*, The role of graphene oxide content on the adsorption-enhanced photocatalysis of titanium dioxide/graphene oxide composites, *Chem. Eng. J.*, 2011, **170**, 226–232.
- 68 P. J. Mafa, M. E. Malefane, A. O. Idris, *et al*, Multi-elemental doped g-C<sub>3</sub>N<sub>4</sub> with enhanced visible light photocatalytic pctivity: insight into naproxen degradation, kinetics, effect of electrolytes, and mechanism, *Sep. Purif. Technol.*, 2022, **282**, 120089.
- 69 F. Khan, M. S. Khan, S. Kamal, *et al*, Recent advances in graphene oxide and reduced graphene oxide based nanocomposites for the photodegradation of dyes, *J. Mater. Chem. C*, 2020, **8**, 15940–15955.
- 70 A. L. T. Zheng, S. Sabidi, T. Ohno, T. Maeda and Y. Andou, Cu<sub>2</sub>O/TiO<sub>2</sub> decorated on cellulose nanofiber/reduced graphene hydrogel for enhanced photocatalytic activity and its antibacterial applications, *Chemosphere*, 2022, **286**, 131731.

